BIOMIMETICS

Copyright © 2020 The Authors, some rights reserved; exclusive licensee American Association for the Advancement of Science. No claim to original U.S. Government Works

A bioinspired Separated Flow wing provides turbulence resilience and aerodynamic efficiency for miniature drones

Matteo Di Luca[1]*, Stefano Mintchev[2], Yunxing Su[1], Eric Shaw[1], Kenneth Breuer[1]

Small-scale drones have enough sensing and computing power to find use across a growing number of applications. However, flying in the low–Reynolds number regime remains challenging. High sensitivity to atmospheric turbulence compromises vehicle stability and control, and low aerodynamic efficiency limits flight duration. Conventional wing designs have thus far failed to address these two deficiencies simultaneously. Here, we draw inspiration from nature's small flyers to design a wing with lift generation robust to gusts and freestream turbulence without sacrificing aerodynamic efficiency. This performance is achieved by forcing flow separation at the airfoil leading edge. Water and wind tunnel measurements are used to demonstrate the working principle and aerodynamic performance of the wing, showing a substantial reduction in the sensitivity of lift force production to freestream turbulence, as compared with the performance of an Eppler E423 low–Reynolds number wing. The minimum cruise power of a custom-built 104-gram fixed-wing drone equipped with the Separated Flow wing was measured in the wind tunnel indicating an upper limit for the flight time of 170 minutes, which is about four times higher than comparable existing fixed-wing drones. In addition, we present scaling guidelines and outline future design and manufacturing challenges.

INTRODUCTION

Small-scale drones that are intrinsically safe for users and easy to transport and deploy are disrupting commercial and recreational applications ranging from inspection to mapping, environmental monitoring, agriculture, and aerial photography (*1*). Although the availability of submillimeter electronic components is facilitating the development of smaller and lighter autonomous drones (*2*–*6*), Miniature and Nano Air Vehicles (MAVs and NAVs) face two major problems: short flight duration and poor control characteristics due to high sensitivity to wind gusts and atmospheric turbulence.

The short flight duration stems from poor aerodynamic and propulsive efficiency, both of which decrease with vehicle size (*1*, *7*, *8*). As illustrated in Fig. 1A, the flight endurance of existing fixed-wing drones with a weight on the order of 10 to 100 g is typically less than 30 min. Scale effects can be characterized by the Reynolds number, *Re*, a nondimensional parameter defined as $Re = \rho Uc/\mu$, where ρ is the air density, μ is the viscosity of air, *U* is the flight speed, and *c* is the wing chord. The Reynolds number represents the relative importance of inertial to viscous forces in aerodynamic flows, and at low values ($Re < \sim 50{,}000$), aerodynamic efficiency typically declines (*9*, *10*).

Small-scale fixed-wing aircraft are also very sensitive to atmospheric conditions. The aerodynamic lift force depends strongly on the changes in effective air speed: $L = 0.5\rho U^2 S C_L$, where ρ is the air density, *S* is the wing area, and C_L is the nondimensional coefficient of lift. C_L is also strongly dependent on the angle of attack (*11*). MAVs and NAVs flying outdoors frequently experience high-amplitude, large-scale wind fluctuations ("gusts") often as high as 30% of the vehicle's flight speed (*12*). These gusts contribute to changes in both the effective air speed and the effective angle of attack, causing marked and dangerous fluctuations in the aerodynamic lift.

Distinct from the effects of gusts, the lift production in MAVs and NAVs is also sensitive to variations in freestream atmospheric turbulence, *Tu*, which is characterized by broad-band velocity fluctuations and vortical eddies and associated with unsteady atmospheric conditions as well as turbulence in the wakes of obstacles, such as buildings or trees. Freestream turbulence also strongly affects the wing lift coefficient, C_L, primarily by influencing the location and extent of boundary layer separation over the wing (*13*, *14*). In the low Reynolds regime, the flow separates from the airfoil and creates a separation bubble that usually closes if the separated boundary layer transitions to turbulence. Under conditions with low freestream turbulence, the transition process is slow, resulting in a large or open separation bubble (Fig. 1C), which greatly reduces the wing lift (*15*). In contrast, the presence of elevated levels of freestream turbulence greatly shortens the transition distance, reduces the size of the separation bubble (Fig. 1D), and increases the wing lift coefficient.

Thus, MAVs are highly sensitive to both atmospheric gusts and freestream turbulence levels, which can initiate sudden and violent variations in lift forces, making the drone difficult to control (*12*) and subject to mechanical stress and failure. This sensitivity represents a major limitation for operation of MAVs and NAVs outdoors, where the oscillations are exacerbated by the low mass and inertia of these small vehicles.

Increasing both resistance to atmospheric turbulence and flight duration is challenging in the low Reynolds regime because each goal favors substantially different wing designs. Aircraft designers can increase robustness to atmospheric turbulence in several ways. First, a low–aspect ratio wing—where the aspect ratio is the ratio of the wingspan to chord, $AR = b/c$—can increase the local chord Reynolds number above the critical threshold (*9*), thus decreasing the sensitivity of the lift coefficient to turbulence. Second, flexible airfoils can passively dampen the unsteady forces and moments

[1]School of Engineering, Brown University, 182 Hope Street, Providence, RI 02912, USA. [2]Institute of Microengineering, School of Engineering, École Polytechnique Fédérale de Lausanne, 1015 Lausanne, Switzerland.
*Corresponding author. Email: matteo_di_luca@brown.edu

Downloaded from http://robotics.sciencemag.org/ at HANGZHOU DIANZI UNIVERSITY on July 1, 2021

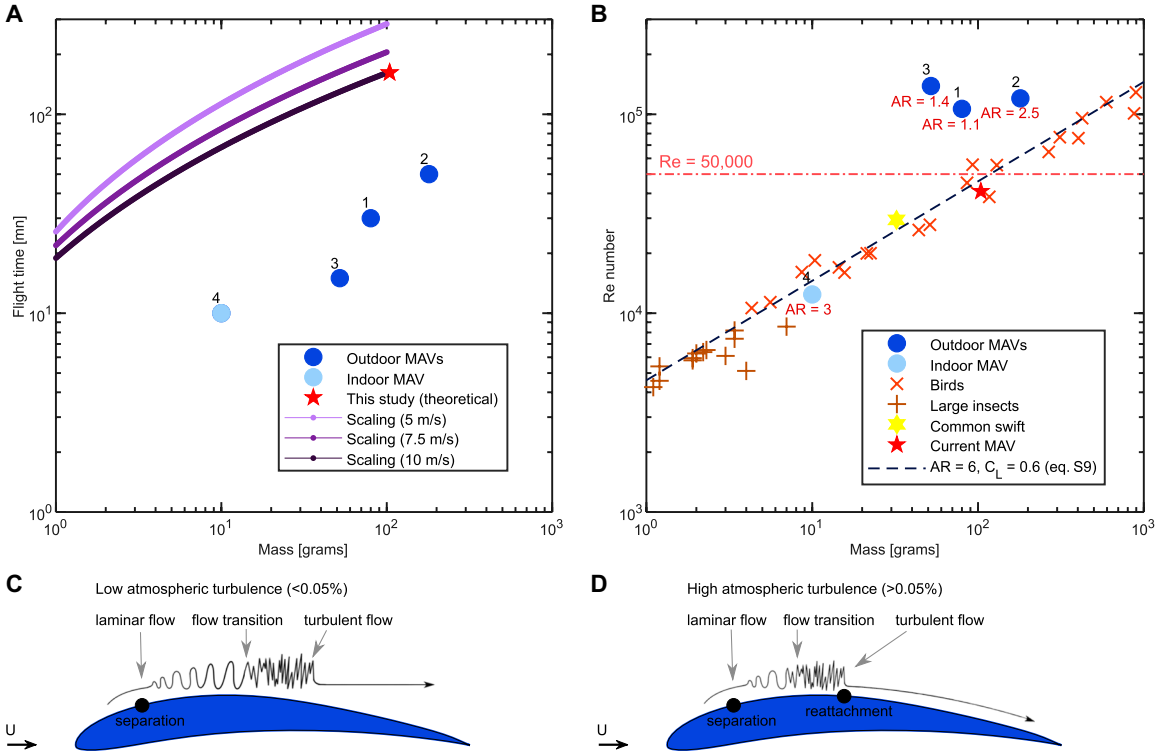

Fig. 1. Endurance, Reynolds number for MAVs and natural flyers, and the effect of atmospheric turbulence on laminar separation. (**A**) The flight time of existing commercial and research fixed-wing MAVs and NAVs (blue and light blue circles) is below 40 min. Lines represent estimated maximum flight times obtained using the scaling analysis in section S2 for flight speeds of 5 m/s (light purple), 7.5 m/s (purple), and 10 m/s (dark purple). (**B**) Most of the existing outdoor MAVs have higher *Re* and smaller *AR* (reported in red) than birds and large insects of comparable mass. The dashed dark blue reference line represents how the *Re* of a vehicle equipped with an *AR* = 6 wing and flying at C_L = 0.6 scales with mass (eq. S9). (**C** and **D**) Below *Re* = 50,000, external turbulence has a high impact on wings with thick airfoil sections (*U* is the wind speed). Comparison fixed-wing vehicles: [1] Black Widow (*35*), [2] Wasp (*40*), [3] University of Florida MAV (*41*), and [4] EPFL MC2 (*42*).

generated by the aerodynamic disturbances (*16*). However, structural concerns constrain the use of flexible structures to low–aspect ratio wings. Last, very thin wings (thickness/chord, <3%) and slightly cambered (i.e., 4%) airfoil sections have more robust and superior aerodynamic performance even in turbulent regimes (*15*, *17*, *18*). However, such airfoils are also limited to low aspect ratios to prevent flexural overloading.

All three of these solutions drive the design of outdoor MAVs toward low–aspect ratio wings (*AR* < 4) (Fig. 1B). However, the vehicle aerodynamic efficiency is strongly affected by wing aspect ratio (see section S3), and thus, designers can either achieve efficient flight with high aspect ratio wings and thick airfoils or develop less efficient thin and flexible low–aspect ratio wings to fly outdoors or under turbulent atmospheric conditions (Fig. 1B). At low Reynolds numbers, conventional wing designs cannot achieve both flight characteristics simultaneously.

Robust lift production can, however, be achieved without sacrificing aerodynamic efficiency by studying natural flyers such as large insects and small birds. Insect wings dictate the location of separation at or very near to the leading edge using sharp leading edges and corrugated wings (*19*–*21*). At Reynolds numbers in the range of 10,000 to 70,000, the feathered leading edge surfaces on wings of small bird such as swifts (*22*, *23*) and hummingbirds (*24*) have protrusions [roughness height up to 2% of the chord (Fig. 2A)] that either force separation at the leading edge or induce localized regions of incipient laminar separation. Early flow separation facilitates rapid transition to turbulence; the resultant turbulent flow is resistant to large-scale separation from the wing back region (*22*) and preserves good aerodynamic performance over a range of operating conditions.

Here, we present a wing design principle that takes inspiration from these natural fliers to make the flow separation and laminar-turbulent transition robust to gust disturbances and variations in freestream turbulence. In the proposed "Separated Flow" airfoil, the benefits of the complex surface architecture of natural wings are achieved using a simple design composed of a thick flat plate and a rounded back flap (Fig. 2B). The sharp leading edge of the flat plate forces a sudden separation of the laminar flow. The separated flow is characterized by an unstable shear layer (*20*, *25*) that completes a rapid transition to turbulence within a short fraction of the chord. Unlike the flow over a simple flat-plate wing, the rounded flap near the trailing edge facilities the reattachment of the shear layer, which aids in closing the separation bubble to maximize lift generation.

As discussed earlier, in conventional airfoils, the location of the laminar-turbulent transition is strongly influenced by the level of atmospheric turbulence (Fig. 1, C and D). In contrast, on the proposed airfoil, the separation point is clearly defined, and the transition to turbulence is consistently achieved before the flow reaches the back flap. As a result, lift generation should be insensitive to external turbulence, hence allowing the integration of the airfoil into energetically efficient high–aspect ratio wings.

In addition to its aerodynamic benefits, the Separated Flow wing has other appealing qualities. The design allows for a relatively thick

Downloaded from http://robotics.sciencemag.org/ at HANGZHOU DIANZI UNIVERSITY on July 1, 2021

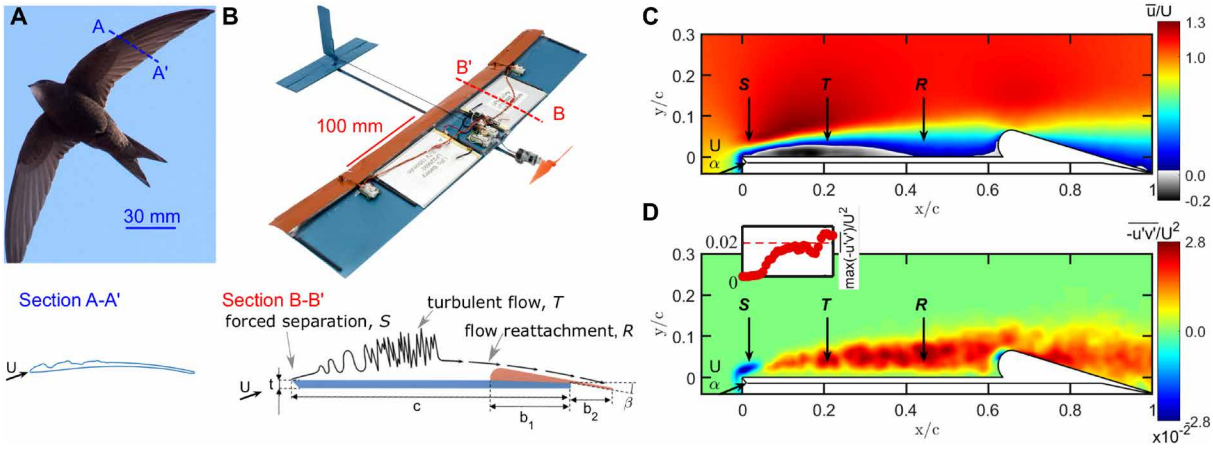

Fig. 2. Separated flow airfoils in natural flyers and for MAVS. (**A**) The surface roughness on the wing of the common swift facilitates flow separation promoting transition to turbulence for more resilient performance across different Reynolds regimes and angles of attack (*23*). Airfoil section reprinted from (*23*). (**B**) Photograph of the 104-g MAV demonstrator and a section of the bioinspired Separated Flow airfoil. The top surface of the wing is removed to highlight the integration of batteries and electronics inside the wing. (Bottom) A section of the bioinspired Separated Flow airfoil illustrates the flat plate (in blue) and the rear flap (in red). The flow separates at the sharp leading edge, transitions to turbulence, and reattaches over the flap. c is the airfoil chord, t is the bottom plate thickness, b_1 and b_2 are the lengths of the flap portions fore and aft of the bottom plate trailing edge, and β is the flap angle. (**C**) The time averaged horizontal velocity field, $\overline{u}/U$, captured over the wing mid-span plane, using PIV in a water tunnel, illustrates the airfoil aerodynamic principle (Re = 40,000, α = 5°, Tu = 2.5%). Near the leading edge, a region of negative speed (fluid moving toward the leading edge) marks the presence of flow separation, S. After transitioning to turbulence, T, the flow reattaches, R, over the plate as speed increases near the surface. The boundary layer travels over the flap leading edge and remains attached over the back. (**D**) Soon after separation, the Reynolds stress, $\overline{-u'v'}/U^2$, grows, as shown by the evolution of the maximum values along y/c, indicating the transition to turbulence of the separated shear layer (*23*, *39*).

airfoil geometry that allows for the fabrication of high–aspect ratio wings. The flat-plate geometry eliminates the necessity for a carefully contoured airfoil shape and can be easily manufactured. Subsystems—such as batteries, antennas, and solar cells—can be directly integrated into the wing surface, reducing the required structural mass and potentially eliminating the need for a fuselage (*26*).

In the following sections, we describe the working principle of the Separated Flow wing and then quantify, using flow and force measurements from water and wind tunnel tests, the wing's aerodynamic properties and its resilience to freestream turbulence. Following this, we present a fully functional 104-g demonstrator MAV (Fig. 2B) and measure the power required for equilibrium flight, showing that a flight time of almost 3 hours is possible—a substantial improvement over existing MAV systems. Last, we discuss the scalability of the design, including the performance versus weight of the aerodynamic subsystem as well as the battery, propeller, and motor subsystems.

RESULTS

Airfoil working principle

The working principle of the Separated Flow wing—forced flow separation at the leading edge, followed by transition to turbulence and reattachment over the rear flap—was validated using particle image velocimetry (PIV) in a water tunnel testing facility. Figure 2C shows the average horizontal velocity flow field, $\overline{u}/U$, at Re = 40,000 and angle of attack α = 5°. After flow separation (S) at the leading edge (reverse flow is indicated by the gray-black colors in Fig. 2C), the shear layer transitioned from laminar to turbulent (T), indicated by the rise in the Reynolds stress (Fig. 2D), and flow reattachment (R) occurred slightly ahead of the flap leading edge. The turbulent boundary layer remained attached over the back of the flap. Increasing the angle of attack moved reattachment closer to the flap leading edge (fig. S4, A and B) and only marginally affected the transition location (fig. S4C).

Wing aerodynamic performance measurements

The lift coefficient, C_L, and the efficiency of the Separated Flow wing, defined as lift-to-drag ratio, C_L/C_D, were compared to the efficiency of the reference wing based on the Eppler E423 airfoil—a cambered low–Reynolds number airfoil appropriate for MAVs (*27*). The aspect ratio of the two wings was the same (5.3). Force measurements at Re = 40,000 confirmed the expected high sensitivity to external turbulence of the Eppler wing (Fig. 3A, blue symbols), most markedly indicated by the extreme difference between the maximum value of the lift coefficients achieved in the low-turbulence (Tu = 0.04%) and high-turbulence (Tu = 6.9%) airstreams. Moreover, at the intermediate turbulence level, Tu = 1.1%, marked lift variations could occur with very small changes in the angle of attack.

Freestream turbulence levels also affected wing efficiency, with variations as high as 125% (Fig. 3B, blue symbols). The behavior persisted at lower Reynolds number, Re = 20,000 (fig. S1, A and B).

In contrast to the conventional wing, the Separated Flow wing showed only minor sensitivity to external turbulence at all angles of attack (Fig. 3, A and B, red symbols). Both lift and efficiency were only slightly affected (degraded) by the presence of external turbulence. Although the Separated Flow wing did not achieve as high a maximum level of C_L as the Eppler wing at high turbulence levels, it showed better efficiency, 5.7 versus 4.1, at low freestream turbulence levels.

One possible metric of turbulence resilience is the percentage change in the maximum lift in the presence of freestream turbulence. For the Separated Flow wing, the increase in maximum lift was less than 13% at Re = 40,000, whereas the increase in lift for the Eppler wing was more than 85% (Fig. 3A).

Hot wire measurements of the boundary layer velocity profiles around the Eppler and Separated Flow wings demonstrated the effects

Downloaded from http://robotics.sciencemag.org/ at HANGZHOU DIANZI UNIVERSITY on July 1, 2021

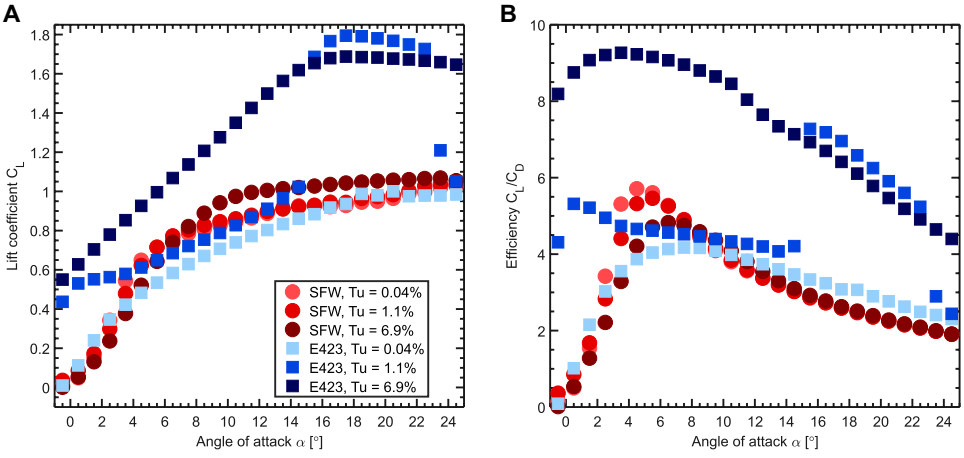

Fig. 3. Lift production and performance resilience to turbulence. (**A**) A high increase in lift coefficient, C_L, results from variations in external turbulence levels, *Tu*, for an Eppler E423 wing at *Re* = 40,000 (blue symbols). The variation is dependent on the level of external turbulence and on the angle of attack. The Separated Flow wing is relatively insensitive to external turbulence levels (red symbols). (**B**) High levels of external turbulence result in a great variation (improvement) of wing efficiency, C_L/C_D, for the Eppler E423 wing compared with only a minor change (degradation) for the Separated Flow wing.

of freestream turbulence on the flow over the wing and the subsequent lift coefficient. At low turbulence levels, Tu = 0.04%, the velocity profiles around the Eppler wing indicated an extensive region of flow separation starting at $x/c \approx 40\%$ and extending past the wing trailing edge (Fig. 4A). Separation was eliminated when external turbulence increased (Tu = 6.9%; Fig. 4B), which allowed lower pressure to be maintained over the airfoil (*28*) and increased C_L by 80% from 0.63 to 1.13 (α = 8°, Fig. 3A).

An increase in external turbulence moved both the transition, *T*, and reattachment, *R*, points on the Separated Flow wing forward, toward the Leading Edge, as shown at the angle of attack of maximum efficiency, α = 5° in Fig. 4, C and D. The increased freestream turbulence only slightly affected the overall size of the separated region. These modest effects on the velocity distribution around the airfoil (fig. S5A) have minimal effects on the lift and drag. Earlier transition and reattachment and similar effects on the speed distribution were also observed at higher angles of attack (figs. S6 and S5B).

Vehicle design and power consumption

The Separated Flow wing was integrated into a self-contained demonstration drone (details in Materials and Methods) to provide a measure of the maximum theoretical flight time and the impact of external turbulence on it. The vehicle (Fig. 5, A and B, and table) is composed of the Separated Flow wing, a rear tail, a front-mounted propulsion unit (motor, gearbox, and propeller), batteries, and electronics for control. The size of the vehicle was dictated by the availability of a wide selection of commercial off-the-shelf components appropriate for a vehicle of this scale.

Several design features are worth noting. The relatively thick (8.5%) and flat airfoil not only provided the desired flight performance and turbulence resilience but also allowed for high aspect ratio and easy integration of the batteries and control servos (Fig. 5, A and B). Two lithium polymer batteries occupied 23% of the wing volume. The flight control receiver and the ailerons/elevator servomotors were also integrated in the wing. The thick wing provided structural strength, which allowed for the high aspect ratio design, increasing the vehicle lift-to-drag ratio and providing considerable power savings and longer endurance flight at low cruise speeds (for a given weight).

The demonstration MAV was successfully flown in the field (movie S1). However, because a long-duration flight in the field was not practical for this research-grade vehicle, the flight endurance was estimated from the propulsion power required for horizontal flight, which we measured in a controlled wind tunnel environment. The power consumption of the propulsion unit (propeller, gearbox, and motor) was measured over a range of freestream velocities (Fig. 5C). At both high and low levels of freestream turbulence, the power curves exhibited a minimum close to 6.5 m/s. High levels of freestream turbulence (Tu = 6.9%) tended to increase the required propulsive power, particularly at high flight speeds.

At a flight speed of 7 m/s, and low external turbulence, Tu = 0.04%, the power required by the propulsion unit (motor and propeller) to fly at equilibrium conditions was 3.5 W. The total power consumption (including losses in the control electronics and actuation power) was estimated to be 3.8 W, and the minimum current drawn by the motor and the electronics was 1.5 A. Under this load condition, the measured total capacity for each battery is 5390 mWh (see section S6), and with two batteries connected in parallel, the maximum flight time is estimated to be 170 min. At the higher level of freestream turbulence, in the speed region of minimum power, 6.3 to 6.8 m/s, the required increase in power was about 10% above that of the low turbulence condition, resulting in an estimated flight time of 155 min.

Scalability

Wind tunnel tests show that lift generation was only slightly affected by external turbulence also at *Re* = 20,000 (<13%; fig. S1A) and *Re* = 10,000 (fig. S1B). For comparison, the increase in the Eppler wing was more than 62% at *Re* = 20,000. Therefore, the Flow Separated wing also maintains a consistent external turbulence resilience if used for MAVs with a mass below 100 g (Fig. 1B).

The scaling of an electric flying vehicle flight time with its mass can be studied starting from the flight time expression

$$\text{Flight time} = \eta_{\text{con}}\ \eta_{\text{p}}\ e_{\text{spec battery}}\ \frac{C_L}{C_D}\ \frac{W_{\text{battery}}}{W_{\text{vehicle}}}\ \frac{1}{U\ 60}\quad [\text{min}] \tag{1}$$

where η_{con} is the control electronics efficiency, η_{p} is the propulsion efficiency (motor, propeller, and gearbox), $e_{\text{spec battery}}$ is the specific energy of batteries (in joules per newton), C_L/C_D is the aerodynamic efficiency of the wing, $W_{\text{battery}}/W_{\text{vehicle}}$ is the battery weight fraction, and *U* the cruise speed (in meters per second). The derivation of this equation is provided in section S2, and flight times for a range of small flight vehicles at three different speeds are shown in Fig. 1A. Note that although small-scale drones with low–aspect ratio wings exhibit flight times in the 10- to 40-min range, the current design

Downloaded from http://robotics.sciencemag.org/ at HANGZHOU DIANZI UNIVERSITY on July 1, 2021

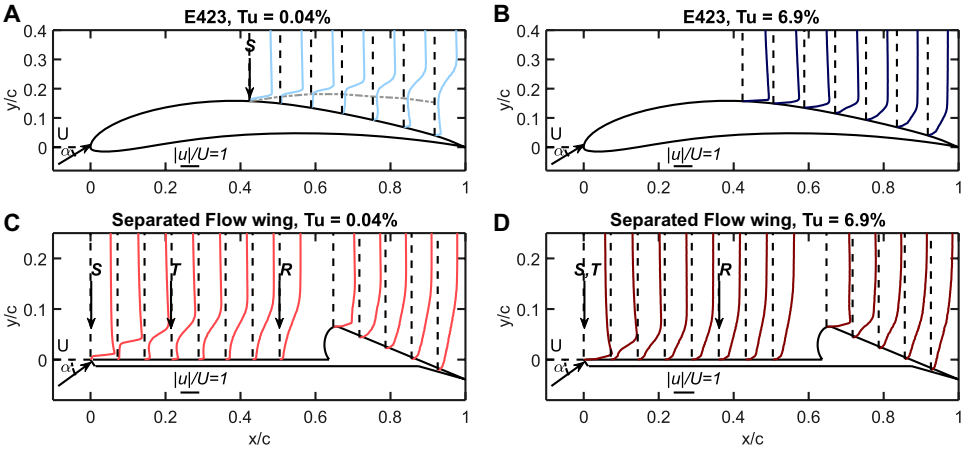

Fig. 4. Atmospheric turbulence has only a minor effect on the flow field of the Separated Flow wing compared with the Eppler wing. The continuous lines and the black dashed lines represent the local velocity and the zero velocity at each chord-wise station. (**A**) Under conditions of low turbulence, Tu = 0.04%, flow separation occurs along more than half of the E423 wing as indicated by the zero speed contour line (gray dashed line). (**B**) Increased turbulence, Tu = 6.9%, eliminates separation, causes higher speeds in the leading edge region and a C_L increase of 80% from 0.63 to 1.13 ($\alpha = 8^\circ$; Fig. 3A). (**C**) Under the condition of wing maximum efficiency, $\alpha = 5^\circ$, with low external turbulence, Tu = 0.04%, the separated flow transitions to turbulent, T, at about one-fifth of the chord (the criteria for determining the transition location is described in Materials and Methods). (**D**) With increased external turbulence, Tu = 6.9%, transition occurs very close to the leading edge, reattachment, R, occurs earlier, and the separation region is smaller. However, the change in the flow field and the speed distribution around the airfoil is only minor (fig. S5A) and results in a small lift variation (Fig. 3).

has an estimated flight time of maximum 170 min (red star in Fig. 1A), based on the result of the wind tunnel flight power tests described above.

DISCUSSION

Benefits of the Separated Flow wing

The test results demonstrate that the Separated Flow airfoil design, although unconventional, greatly improved the wing's resilience to freestream turbulence levels. Although the maximum aerodynamic efficiency is lower than that of a conventional low-Re section in the presence of turbulence (Fig. 3B), the performance was largely unaffected by both freestream turbulence levels (Fig. 3A) and changes in Reynolds number (fig. S1).

We did observe a relatively minor reduction in lift due to external turbulence at $\alpha < 8^\circ$ (Fig. 3), which can be explained by looking at the structure of the separated flow over the wing. At Tu = 0.04%, transition requires ≈20% of the chord, whereas at Tu = 6.9%, it occurs right after separation (Fig. 4, C and D). A high level of freestream turbulence results in an faster transition and consequently an earlier reattachment and a shorter separation bubble. This explains the higher maximum speed at the leading edge and the more rapid speed recovery in the presence of high external turbulence levels (fig. S5, A and B). Overall, the earlier reattachment results in a decrease in velocity (and an increase in pressure) over the plate area. As a result, when atmospheric turbulence is high, the average pressure over the top of the plate is increased, and the lift is reduced. Nevertheless, despite these minor variations, the Separated Flow wing provides significantly more robust lift production when compared with the Eppler reference wing (Fig. 3).

For practical drone design, this has notable appeal. Although cruise conditions might enjoy low levels of freestream turbulence, marked changes in freestream turbulence levels are endemic to low-altitude flight in cluttered environments, due to vehicle encounters with the turbulent wakes from buildings, vegetation, etc. At low Reynolds numbers typical for drones, conventional wings, such as the E423 tested here, can experience violent changes in the lift and drag coefficients (Fig. 3A) due to the changes in the behavior of the separated flow over the wing (Fig. 4, A and B), and these changes in aerodynamic forces make the vehicle difficult to control.

At the intermediate turbulence level tested, marked lift variations can also occur with very small changes in the angle of attack for the conventional low-Re section. In contrast, the consistent, predictable performance of the Separated Flow wing to changes in angle of attack (Fig. 3A) and changes in Reynolds number (fig. S1) also provides the wing with superior resilience to low-frequency gusts, which have the effect of changing the effective mean incidence angle and flight Reynolds number.

Nevertheless, the maximum aerodynamic efficiency of the Separated Flow airfoil, C_L/C_D, is still lower than that of a carefully contoured conventional airfoil, such as the E423 (Fig. 3B), and thus, it is perhaps unexpected that our drone demonstrator is predicted to achieve flight times in excess of 150 to 170 min—about four to five times better than flight times demonstrated by existing MAVs (Fig. 1A). The source of this improvement comes from the fact that, although the sectional airfoil performance of the Separated Flow wing is degraded, the overall performance of the wing is improved because of its high aspect ratio, and this strongly affects the flight time (Eq. 1). Unconstrained by the requirements of conventional contoured wing aerodynamics, which drive wing designs toward thin low–aspect ratio wings, the relatively thick design of the Separated Flow wing provides the structural strength for us to reap the efficiency benefits of a high–aspect ratio wing (a detailed analysis of the main factors influencing wing efficiency can be found in section S3).

Drones using a Separated Flow wing also achieve other collateral benefits. A more conventional aircraft design would require the addition of a fuselage to house the functional components, especially the cumbersome batteries. On the contrary, the Separated Flow wing is easy to fabricate and enables battery integration into the wing, which allows for a high battery mass fraction (54% in the current drone design) without the need for a fuselage, which adds weight and drag penalties. Moreover, MAV wind tunnel testing revealed a 20 to 30% lift increase as the high-speed airflow generated by the propeller impinges on the central section of the wing (section S7 and fig. S7).

Moving to even smaller drones, wind tunnel tests also show that the aerodynamic efficiency of the Separated Flow wing scales favorably as it remains consistent at Re = 20,000 and Re = 10,000 (fig. S1C). The cruise speed is mainly dictated by the mission requirements,

Downloaded from http://robotics.sciencemag.org/ at HANGZHOU DIANZI UNIVERSITY on July 1, 2021

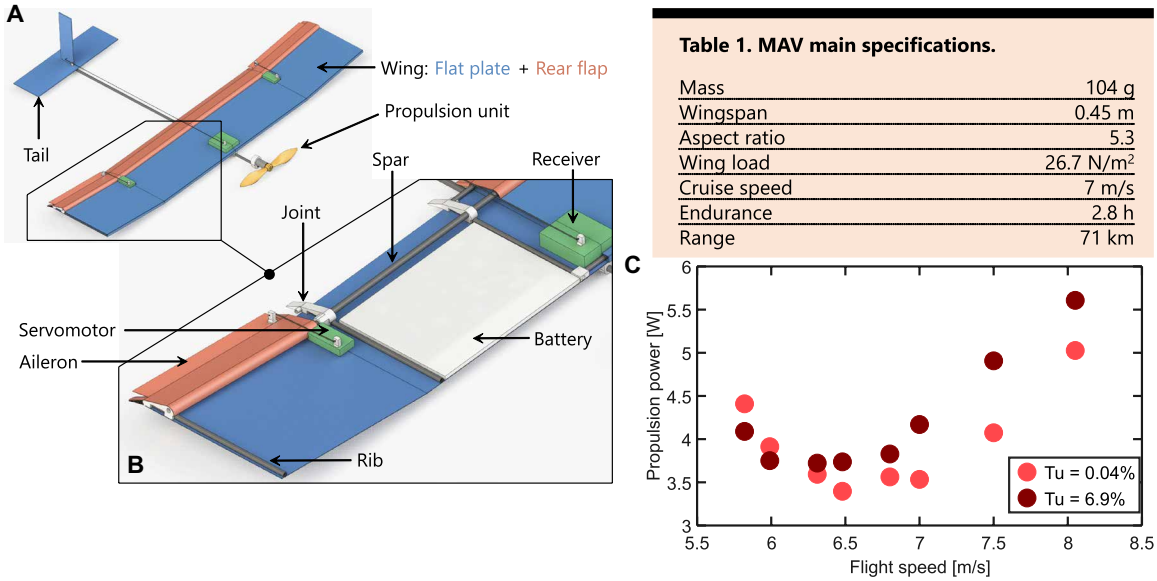

Table 1. MAV main specifications.

Mass	104 g
Wingspan	0.45 m
Aspect ratio	5.3
Wing load	26.7 N/m^2
Cruise speed	7 m/s
Endurance	2.8 h
Range	71 km

Fig. 5. MAV implementation and power required for cruise flight. (**A**) 3D model of the MAV and its main subsystems. (**B**) Detailed view of the wing structure. The top cover and a section of the flap are removed to show the structural and functional components. (**C**) The propulsion power required for flight as measured in the wind tunnel at two turbulence levels. In the speed region for minimum power, atmospheric turbulence tends to increase the power by less than 10%, and the increase is due to a reduction in wing efficiency with external turbulence (Fig. 3B). To estimate the flight time, we add receiver losses and servomotor consumption to obtain the total power required in cruise flight (see Materials and Methods).

whereas what drives the flight time down is the unfavorable scaling of the propulsion efficiency, battery weight fraction, and battery energy density (see section S2.1 for details), all of which present the main constraints for flight endurance in vehicles with a mass below 100 g.

Energetics of the current drone demonstrator

It is important to acknowledge that the flight time estimated from the wind tunnel power measurements has to be considered as an upper theoretical limit for the specific MAV prototype tested. Although the drone tested here is a fully functional vehicle (Fig. 2B and movie S1), it was not robust enough and did not include an autopilot and supporting control systems to allow for a "true" outdoor long-endurance flight test. Hence, we were forced to measure power consumption and to estimate flight endurance based on equilibrium flight (weight support; thrust equals drag) in a wind tunnel environment.

The actual flight time will depend also on aspects not captured by the method, for example, turning maneuvers and wind gusts rejections, that will increase power consumption. On the other hand, we believe that the current theoretical limit could be improved by refining the Separated Flow wing concept. First, the airfoil aerodynamic efficiency could be improved and would greatly benefit from a design optimization with proper modeling of the laminar separation bubble behavior at the low Reynolds numbers. Second, as detailed in section S3, the aerodynamic efficiency is a strong function of the wing aspect ratio, which could be further increased before the structural weight penalty associated with a slender wing would offset the aerodynamics benefits. Third, the current prototype suffers from unnecessary parasitic drag due to the relatively simplistic integration of subsystems (ailerons, linkages, propulsion, servos, receiver, etc.), which could be reduced with more extensive system integration. This would increase the aerodynamic efficiency and consequently further extend the vehicle flight time.

Concluding remarks

The promising performance of this biologically inspired Separated Flow wing concept motivates future research to address remaining design and manufacturing challenges. Because flow separation, transition to turbulence, and reattachment are intrinsically unsteady aerodynamic phenomena, current modeling tools are not suited to predict aerodynamic performances (see section S4), and currently, the only practical design strategy is experimental wind tunnel testing. Preliminary design guidelines for relatively thick (thickness-to-chord ratio, >20%) Separated Flow wings have been reported in (*29*) (see also section S4), although further investigations are necessary to verify their validity for the airfoils used in MAVs and NAVs. Tools to design Separated Flow wings would allow to optimize their aerodynamic performance. For example, controlling the airfoil pitching moment would increase the scope for payload integration in the wing. Currently, pitch stability requires the center of mass of the MAV to be placed at about 33% of the chord aft of the wing leading edge and therefore limits the fraction of heavy components installed in the wing. Moreover, the use of top-down fabrication strategies, for example, origami-inspired manufacturing, is expected to facilitate the integration of components inside the wing and enable new functionalities like morphing (*30*) and mechanical resilience (*31*, *32*) while reducing manufacturing costs (*33*).

Despite these challenges, the marked reduction in the drone's sensitivity to atmospheric turbulence and the increase in the theoretical flight endurance limit open the door to the increased use of miniature and nanodrones in applications that are currently solely the prerogative of larger and heavier vehicles, with benefits in terms of safety, portability, and cost reduction.

Downloaded from http://robotics.sciencemag.org/ at HANGZHOU DIANZI UNIVERSITY on July 1, 2021

MATERIALS AND METHODS

Wing and MAV design and manufacturing

The Separated Flow wing used for aerodynamic testing was manufactured from an aluminum plate with a beveled sharp leading edge and a three-dimensional (3D)–printed back flap (FormLabs2). The resulting wing has a 45-cm wingspan and a 8.5-cm chord length, which corresponds to an aspect ratio AR = 5.3. The Eppler E423 wing was 3D-printed with the same chord, span, and aspect ratio as the Separated Flow wing.

The specific airfoil geometry presented in the current manuscript was derived through an optimization process (details in section S4). The airfoil shape is defined by four main parameters: the relative thickness of the flat plate (t/c), the relative lengths of the flap fore and aft of the trailing edge (b_1/c and b_2/c), and the flap angle (β) (Fig. 2B). To limit the extent of the optimization space, we kept the radius of the rounded flap leading edge surface constant. Combinations of flap angles (β) and relative flap lengths (b_1/c and b_2/c) were explored, subject to the constraint that airfoil maximum relative thickness (t/c) was always higher than 7%, so as to facilitate the integration of functional components into the wing. The final airfoil geometry presented here was selected from among 20 geometries tested in the wind tunnel (details in section S4).

For the MAV implementation, the Separated Flow wing was made with a carbon fiber spar and six ribs connected with 3D-printed joints. The six carbon fiber ribs spaced along the span reinforce the structure and transfer the aerodynamic loads to the main spar. The structure of the wing is covered with 0.2-mm glass fiber sheets that constitute the top and bottom surface of the flat plate. A plastic film connected between the top and bottom surfaces creates the sharp leading edge that forces flow separation. The back flap was also made using a 0.2-mm glass fiber sheet. The external portions of the flap aft of the trailing edge pivot around the trailing edge (Fig. 5, A and B) and function as ailerons for roll torque generation (see section S8).

The front of the vehicle is equipped with an electric propulsion unit. The propeller was chosen from the University of Illinois Urbana-Champaign database (*34*), whereas the motor was selected from a pool of commercially available motors to maximize the propulsive efficiency under cruise condition. The propulsion unit is powered by an 85 mm by 20 mm brushed coreless DC motor (Chaoli) regulated by the speed controller integrated directly in the receiver. A 4:1 gearbox connects the motor to a 100 mm by 80 mm propeller (Plantraco). The nominal maximum propulsive efficiency is close to 50%. At the scale of interest, it is possible to design propellers with efficiency >80% (*35*), and although a custom design would have significantly improved the propulsive efficiency (>15%), this was beyond the scope of the present work.

The radio receiver and power management unit is a Spektrum AS6410L with two integrated Spektrum 1.8-g linear servos controlling the ailerons and rudder. Two additional Spektrum 1.8-g linear servos are embedded in the wing to control the ailerons. Two lithium polymer batteries, Lipol 226693, stored energy onboard.

Wind tunnel testing

For lift and drag measurements, the Separated Flow wing and the Eppler wing were installed on a six-axis force sensor (Nano17, ATI) at the center of the Brown University low-turbulence 1.2 m by 1.2 m wind tunnel test section. The baseline external turbulence levels in the test section were measured using hot-wire anemometry and determined to be 0.05 ± 0.01% at 2 m/s (0.02 %, f > 4Hz) and 0.04 ± 0.005% at 8 m/s (0.02 %, f > 4Hz). To generate elevated turbulence levels, we installed two different rectangular mesh grids into the wind tunnel, upstream of the model [see (*36*) for more details on the methodology]. The high-turbulence grid had rectangular elements d = 3.1 mm in width and spaced 12.7 mm apart. The low-turbulence grid had rectangular elements d = 0.53 mm in width and spaced 5.8 mm apart. At U = 8 m/s, turbulence levels of 6.9 and 1.1% were measured at distances behind the grids of x/d = 80 and 800, respectively.

The force measurements for the Eppler wing and the Separated Flow wing were made on a clean wing, without control surfaces, batteries, etc. All force measurements were repeated three times. Between each measurement, the wind tunnel was turned off, and the model reassembled on the support. SD bars are not shown when they are smaller than the marker size.

The flow field around both the Eppler and Separated Flow wings was measured using a hot-wire anemometer mounted on a 2 degree-of-freedom traverse system with resolution of 12.7 μm per step. The hot wire (5 μm in diameter) was calibrated in the wind tunnel over a speed range of 0 to 12 m/s against a Pitot tube and a high-precision pressure transducer system (MKS Baratron 120 AD). Low-speed readings of the hot wire (below 0.3 m/s) cannot be considered accurate. The streamwise velocity profiles were measured at Re = 40,000 in the plane perpendicular to the wingspan and located at the wing centerline.

Transition to turbulence is determined from the evolution of the streamwise velocity fluctuation power spectra. The fluctuations were recorded with the hot-wire anemometer for 120 s at 17 kHz, at the position in the boundary layer where the local average velocity was half of the maximum speed in the shear layer, $0.5U_{\max\ sl}$. The power spectral densities are computed using the pwelch algorithm in MATLAB (MathWorks) with a frequency resolution of 0.1 Hz. Flow transition was defined as the x/c location where the power spectra displayed a rapid energy increase over a broad range of high frequencies. Boundary layer reattachment is defined as the x/c location where the sharp decrease in the maximum shear layer velocity ends (*37*).

Flight power measurements

The estimation of the power required for sustained horizontal flight starts from the measurement of the propulsion power of the complete MAV model, which includes the presence of control surfaces, electronics, batteries, and propulsion. The vehicle was mounted on the load cell and tested over a range of freestream velocities and at two external turbulence levels Tu = 0.04 and 6.9%. At each freestream velocity, the angle of attack (5° to 12°) and the motor voltage were adjusted until the equilibrium flight condition (lift equals weight and thrust equals drag) was achieved (±0.1 g). The motor current was measured using a shunt resistor. All measurements were repeated three times. SD bars are not shown when they are smaller than the marker size. The total power required for flight was calculated by adding the measured receiver efficiency, η_{con} = 94%, and the power required to actuate the control surfaces servomotors (assuming all three servos are active 10% of the time).

Water tunnel testing

The flow field around the Separated Flow wing—capturing the details of flow separation, transition from laminar to turbulent flow, and reattachment—was measured using PIV. The experiments were carried out in the free-surface circulating water flume at Brown University with an 80 cm by 60 cm test section. The freestream

Downloaded from http://robotics.sciencemag.org/ at HANGZHOU DIANZI UNIVERSITY on July 1, 2021

velocity of U = 0.47 m/s (Re = 40,000) was measured using an Acoustic Doppler Velocimeter (Vectrino, Nortek AS). This facility has a freestream turbulence level, Tu = 2.5%. The flow field around the wing was measured using a 2D PIV system using a single camera (LaVision Imager sCMOS, 2560 pixels by 2160 pixels), a 35-mm lens (Nikon), and a double-pulsed Nd:YAG laser (200 mJ at 532 nm; EverGreen, Quantel USA, MT). The flow was seeded with 50-μm silver-coated hollow ceramic spheres (Potter Industries). The field of view of the camera is 294 mm by 248 mm, with a spatial resolution of about 0.11 mm per pixel. The image pairs of the flow field were acquired at a frame rate of 15 Hz. The velocity vectors were calculated using DaVis v10 (LaVision) using sequential cross-correlations with decreasing interrogation window size (initial size, 48 pixels by 48 pixels; final size, 24 pixels by 24 pixels; 75% overlap).

The instantaneous flow fields obtained were processed to determine the average streamwise and normal velocities, $\overline{u}, \overline{v}$, and the turbulent Reynolds stress, $-\overline{u'v'}$. The average velocity field was computed from 300 instantaneous flow fields, although 200 snapshots were found to be sufficient for convergence.

The location of flow transition from laminar to turbulent is based on the evolution of the maximum Reynolds shear stress in the direction perpendicular to the airfoil chord, $\max(-\overline{u'v'}/U^2)$. Values of the maximum Reynolds stress greater than 0.02 indicate transition to turbulence as also found in the region behind a zigzag roughness strip at low Re numbers (*38*), whereas values in the range of 0.002 to 0.005 correspond to turbulent flow conditions over a flat plate (*23*, *39*).

SUPPLEMENTARY MATERIALS

robotics.sciencemag.org/cgi/content/full/5/38/eaay8533/DC1
Section S1. Reynolds numbers for natural flyers
Section S2. Flight time dependency
Section S3. MAV and NAV aerodynamic efficiency: low or high aspect ratio?
Section S4. Design principles for a Separated Flow airfoil
Section S5. Separated Flow wing working principle, turbulence effects on lift
Section S6. Battery capacity measurement
Section S7. Wing-propeller interaction for lift production
Section S8. Roll control
Fig. S1. Lift coefficient versus angle of attack and maximum efficiency scaling with Reynolds number.
Fig. S2. Subsystem scaling.
Fig. S3. Separated Flow airfoil performance.
Fig. S4. The angle of attack influences the reattachment position and not the distance required for laminar to turbulent transition (Re = 40,000 and Tu = 2.5%).
Fig. S5. Reattachment position of the separated shear layer.
Fig. S6. Velocity profiles around the Separated Flow wing at $\alpha = 7°$, Re = 40,000 and at two turbulence levels.
Fig. S7. Lift increase due to propeller action.
Fig. S8. Ailerons characterization.
Table S1. Airfoil geometries tested in the wind tunnel.
Table S2. The capacity of two different batteries was measured at two different discharge rates.
Movie S1. Video of flight.
Data S1. Reynolds numbers of large insects and small birds.
Data S2. Propellers efficiency and power.
Data S3. Motors efficiency and power output.
Data S4. Lithium polymer batteries–specific energy.
Data S5. Data and scripts used to generate figures.
References (*43*–*56*)

REFERENCES AND NOTES

1. D. Floreano, R. J. Wood, Science, technology and the future of small autonomous drones. *Nature* **521**, 460–466 (2015).
2. K. Y. Ma, P. Chirarattananon, S. B. Fuller, R. J. Wood, Controlled flight of a biologically inspired, insect-scale robot. *Science* **340**, 603–607 (2013).
3. D. Floreano, R. Pericet-Camara, S. Viollet, F. Ruffier, A. Brückner, R. Leitel, W. Buss, M. Menouni, F. Expert, R. Juston, M. K. Dobrzynski, G. L'Eplattenier, F. Recktenwald, H. A. Mallot, N. Franceschini, Miniature curved artificial compound eyes. *Proc. Natl. Acad. Sci. U.S.A.* **110**, 9267–9272 (2013).
4. A. Ramezani, S.-J. Chung, S. Hutchinson, A biomimetic robotic platform to study flight specializations of bats. *Sci. Robot.* **2**, eaal2505 (2017).
5. M. Karásek, F. T. Muijres, C. De Wagter, B. D. W. Remes, G. C. H. E. de Croon, A tailless aerial robotic flapper reveals that flies use torque coupling in rapid banked turns. *Science* **361**, 1089–1094 (2018).
6. M. A. Estrada, S. Mintchev, D. L. Christensen, M. R. Cutkosky, D. Floreano, Forceful manipulation with micro air vehicles. *Sci. Robot.* **3**, eaau6903 (2018).
7. K. Karydis, V. Kumar, Energetics in robotic flight at small scales. *Interface Focus* **7**, 20160088 (2016).
8. A. Noth, Design of solar powered airplanes for continous flight, thesis, ETH Zurich (2008).
9. P. Lissaman, Low-Reynolds-number airfoils. *Annu. Rev. Fluid Mech.* **15**, 223–239 (1983).
10. M. Drela, in *Low Reynolds Number Aerodynamics* (Springer, 1989), pp. 1–12.
11. D. G. Hull, *Fundamentals of Airplane Flight Mechanics* (Springer, 2007).
12. S. Watkins, J. Milbank, B. J. Loxton, W. H. Melbourne, Atmospheric winds and their implications for microair vehicles. *AIAA J.* **44**, 2591–2600 (2006).
13. M. Thompson, S. Watkins, Gust inputs relevant to bees, birds and mavs, in *25th Bristol International Unmanned Aerial Vehicle Systems Conference, Bristol, UK* (2010).
14. J. Tank, B. F. Klose, G. Jacobs, G. R. Spedding, Computer and laboratory studies on the aerodynamics of the NACA 65 (1)-412 at Reynolds number 20 000, in *AIAA SciTech 2019 Forum* (AIAA, 2019), p. 2162.
15. J. Winslow, H. Otsuka, B. Govindarajan, I. Chopra, Basic understanding of airfoil characteristics at low Reynolds numbers (10^4–10^5). *J. Aircr.* **55**, 1050–1061 (2017).
16. P. G. Ifju, D. A. Jenkins, S. Ettinger, Y. Lian, W. Shyy, M. R. Waszak, Flexible-wing-based micro air vehicles, in *40th AIAA Aerospace Sciences Meeting and Exhibit* (AIAA, 2002), pp. 2514.
17. E. V. Laitone, Wind tunnel tests of wings at Reynolds numbers below 70 000. *Exp. Fluids* **23**, 405–409 (1997).
18. W. Shyy, F. Klevebring, M. Nilsson, J. Sloan, B. Carroll, C. Fuentes, Rigid and flexible low Reynolds number airfoils. *J. Aircr.* **36**, 523–529 (1999).
19. R. J. Bomphrey, T. Nakata, P. Henningsson, H.-T. Lin, Flight of the dragonflies and damselflies. *Philos. Trans. R. Soc. Lond. Ser. B Biol. Sci.* **371**, 20150389 (2016).
20. M. Tamai, Z. Wang, G. Rajagopalan, H. Hu, G. He, Aerodynamic performance of a corrugated dragonfly airfoil compared with smooth airfoils at low Reynolds numbers, in *45th AIAA Aerospace Sciences Meeting and Exhibit* (AIAA, 2007), p. 483.
21. C. J. C. Rees, Form and function in corrugated insect wings. *Nature* **256**, 200 (1975).
22. D. Lentink, R. de Kat, Gliding swifts attain laminar flow over rough wings. *PLOS ONE* **9**, e99901 (2014).
23. E. van Bokhorst, R. de Kat, G. E. Elsinga, D. Lentink, Feather roughness reduces flow separation during low Reynolds number glides of swifts. *J. Exp. Biol.* **218**, 3179–3191 (2015).
24. Y. Elimelech, C. P. Ellington, Analysis of the transitional flow field over a fixed hummingbird wing. *J. Exp. Biol.* **216**, 303 (2013).
25. C.-M. Ho, P. Huerre, Perturbed free shear layers. *Annu. Rev. Fluid Mech.* **16**, 365–422 (1984).
26. J. P. Thomas, M. A. Qidwai, The design and application of multifunctional structure-battery materials systems. *J. Miner. Met. Mater. Soc.* **57**, 18–24 (2005).
27. A. R. Jones, N. M. Bakhtian, H. Babinsky, Low Reynolds number aerodynamics of leading-edge flaps. *J. Aircr.* **45**, 342–345 (2008).
28. W. Shyy, Y. Lian, J. Tang, D. Viieru, H. Liu, *Aerodynamics of Low Reynolds Number Flyers* (Cambridge Aerospace Series, Cambridge Univ. Press, 2007), vol. 22.
29. M. Di Luca, K. Breuer, Steady blowing to control the lift and drag on a free shear layer airfoil, in *AIAA SciTech 2019 Forum* (AIAA, 2019), p. 0588.
30. L. Dufour, K. Owen, S. Mintchev, D. Floreano, A drone with insect-inspired folding wings, in *2016 IEEE/RSJ International Conference on Intelligent Robots and Systems (IROS)* (IEEE/RSJ, 2016), pp. 1576–1581.
31. S. Mintchev, J. Shintake, D. Floreano, Bioinspired dual-stiffness origami. *Sci. Robot.* **3**, eaau0275 (2018).
32. P. Sareh, P. Chermprayong, M. Emmanuelli, H. Nadeem, M. Kovac, Rotorigami: A rotary origami protective system for robotic rotorcraft. *Sci. Robot.* **3**, eaah5228 (2018).
33. D. Rus, M. T. Tolley, Design, fabrication and control of origami robots. *Nat. Rev. Mater.* **3**, 101–112 (2018).
34. R. W. Deters, G. K. Ananda, M. S. Selig, Reynolds number effects on the performance of small-scale propellers, in *32nd AIAA Applied Aerodynamics Conference*, Atlanta (AIAA, 2014), pp. 2151.
35. J. M. Grasmeyer, M. T. Keennon, Development of the black widow micro air vehicle, in *39th AIAA Aerospace Sciences Meeting and Exhibit* (AIAA, 2001), p. 0127.
36. P. Roach, The generation of nearly isotropic turbulence by means of grids. *Int. J. Heat Fluid Flow* **8**, 82–92 (1987).

Downloaded from http://robotics.sciencemag.org/ at HANGZHOU DIANZI UNIVERSITY on July 1, 2021

37. G. S. Schmidt, T. J. Mueller, Analysis of low Reynolds number separation bubbles using semiempirical methods. *AIAA J.* **27**, 993–1001 (1989).
38. G. E. Elsinga, J. Westerweel, Tomographic-PIV measurement of the flow around a zigzag boundary layer trip. *Exp. Fluids* **52**, 865–876 (2012).
39. P. Klebanoff, "Characteristics of turbulence in a boundary layer with zero pressure gradient" (Technical Report NACA 1247, NACA, 1955).
40. AeroVironment, Aerovironment Wasp (2019); www.designation-systems.net/dusrm/app4/wasp.html [accessed 23 May 2019].
41. W. Shyy, P. Ifju, D. Viieru, Membrane wing-based micro air vehicles. *Appl. Mech. Rev.* **58**, 283–301 (2005).
42. J.-C. Zufferey, A. Klaptocz, A. Beyeler, J.-D. Nicoud, D. Floreano, A 10-gram vision-based flying robot. *Adv. Robot.* **21**, 1671–1684 (2007).
43. H. Tennekes, *The Simple Science of Flight: From Insects to Jumbo Jets* (MIT press, 2009).
44. The Cornell Lab of Ornithology, Data on bird wings (2019); www.allaboutbirds.org/ [accessed 15 June 2019].
45. G. E. Dorrington, On the scaling of dragonflies, in *10th International Micro-Air Vehicles Conference* (IMAVS, 2018), p. 53.
46. A. E. R. Cannell, The engineering of the giant dragonflies of the permian: Revised body mass, power, air supply, thermoregulation and the role of air density. *J. Exp. Biol.* **221**, jeb185405 (2018).
47. S. A. Cabrera-Cruz, T. J. Mabee, R. V. Patraca, Using theoretical flight speeds to discriminate birds from insects in radar studies. *Condor* **115**, 263–272 (2013).
48. L. C. Johansson, S. Engel, E. Baird, M. Dacke, F. T. Muijres, A. Hedenström, Elytra boost lift, but reduce aerodynamic efficiency in flying beetles. *J. R. Soc. Interface* **9**, 2745–2748 (2012).
49. P. S. Baker, M. Gewecke, R. J. Cooter, The natural flight of the migratory locust, *Locusta migratoria* L. *J. Comp. Physiol.* **141**, 233–237 (1981).
50. D. J. Pines, F. Bohorquez, Challenges facing future micro-air-vehicle development. *J. Aircr.* **43**, 290–305 (2006).
51. J.-C. Zufferey, "Bio-inspired vision-based flying robots," thesis, EPFL (2005).
52. M. Kovac, A. Guignard, J.-D. Nicoud, J.-C. Zufferey, D. Floreano, A 1.5 g sma-actuated microglider looking for the light, in *Proceedings 2007 IEEE International Conference on Robotics and Automation* (IEEE, 2007), pp. 367–372.
53. R. Wood, S. Avadhanula, E. Steltz, M. Seeman, J. Entwistle, A. Bachrach, G. Barrows, S. Sanders, R. S. Fearing, Design, fabrication and initial results of a 2g autonomous glider, in *31st Annual Conference of IEEE Industrial Electronics Society, 2005. IECON 2005* (IEEE, 2005), pp. 8–15.
54. K. D. Chabak, "Conceptual study of rotary-wing microrobotics," thesis, Air Force Institute of Technology (2008).
55. S. Martínez-Aranda, A. L. García-González, L. Parras, J. F. Velázquez-Navarro, C. del Pino, Comparison of the aerodynamic characteristics of the NACA0012 airfoil at low-to-moderate Reynolds numbers for any aspect ratio. *Int. J. Aerospace Sci.* **4**, 1–8 (2016).
56. D. Raymer, *Aircraft Design: A Conceptual Approach* (American Institute of Aeronautics and Astronautics Inc., 2012).

Funding: This work is supported by the NSF, NRI award CMMI-1426338. M.D.L. is supported by a Brown University Presidential Fellowship. **Author contributions:** M.D.L. and K.B. initiated the project. M.D.L. designed, developed, and tested the Separated Flow airfoil. Y.S. and M.D.L. characterized the wing through PIV. E.S. and M.D.L. characterized the wing with force measurements. M.D.L. and S.M. designed the MAV. M.D.L. built and tested the MAV. M.D.L., S.M., Y.S., and K.B. contributed to data analysis and discussion. M.D.L., S.M., and K.B. wrote the paper. K.B. directed the project. **Competing interests:** M.D.L. and K.B. hold a U.S. Provisional Patent on the Separated Flow wing. **Data and materials availability:** All data needed to evaluate the conclusions in the paper are present in the paper or the Supplementary Materials and are available at Zenodo (DOI: 10.5281/zenodo.3598639).

Submitted 28 July 2019
Accepted 9 January 2020
Published 29 January 2020
10.1126/scirobotics.aay8533

Citation: M. Di Luca, S. Mintchev, Y. Su, E. Shaw, K. Breuer, A bioinspired Separated Flow wing provides turbulence resilience and aerodynamic efficiency for miniature drones. *Sci. Robot.* **5**, eaay8533 (2020).

Downloaded from http://robotics.sciencemag.org/ at HANGZHOU DIANZI UNIVERSITY on July 1, 2021

Science Robotics

A bioinspired Separated Flow wing provides turbulence resilience and aerodynamic efficiency for miniature drones

Matteo Di Luca, Stefano Mintchev, Yunxing Su, Eric Shaw and Kenneth Breuer

Sci. Robotics **5**, eaay8533.
DOI: 10.1126/scirobotics.aay8533

ARTICLE TOOLS http://robotics.sciencemag.org/content/5/38/eaay8533

SUPPLEMENTARY MATERIALS http://robotics.sciencemag.org/content/suppl/2020/01/27/5.38.eaay8533.DC1

RELATED CONTENT http://robotics.sciencemag.org/content/robotics/5/38/eaay1246.full
http://robotics.sciencemag.org/content/robotics/2/3/eaal2505.full

REFERENCES This article cites 34 articles, 6 of which you can access for free
http://robotics.sciencemag.org/content/5/38/eaay8533#BIBL

PERMISSIONS http://www.sciencemag.org/help/reprints-and-permissions

Use of this article is subject to the Terms of Service

Science Robotics (ISSN 2470-9476) is published by the American Association for the Advancement of Science, 1200 New York Avenue NW, Washington, DC 20005. The title *Science Robotics* is a registered trademark of AAAS.

Copyright © 2020 The Authors, some rights reserved; exclusive licensee American Association for the Advancement of Science. No claim to original U.S. Government Works

Downloaded from http://robotics.sciencemag.org/ at HANGZHOU DIANZI UNIVERSITY on July 1, 2021